



# Structure–reactivity relationships of Ni–NiO core–shell co-catalysts on Ta<sub>2</sub>O<sub>5</sub> for solar hydrogen production



Qianlang Liu, Liuxian Zhang, Peter A. Crozier\*

School for Engineering of Matter, Transport and Energy, Arizona State University, Tempe, AZ 85287-6106, USA

## ARTICLE INFO

### Article history:

Received 22 October 2014

Received in revised form 4 January 2015

Accepted 9 January 2015

Available online 3 February 2015

### Keywords:

Ni–NiO

Ta<sub>2</sub>O<sub>5</sub>

Core–shell

Co-catalyst

Structure–reactivity relationship

Deactivation

## ABSTRACT

Ni–NiO core–shell co-catalyst structures on Ta<sub>2</sub>O<sub>5</sub> have been investigated for solar H<sub>2</sub> production. Core–shell co-catalysts with different morphologies resulted in large changes in photocatalytic activity. Increased H<sub>2</sub> production was found to be related to an increase in the thickness of NiO shell due to suppression of the back reaction. Atomic level transmission electron microscopy showed that the core–shell co-catalyst structures deactivated primarily due to a loss of metallic Ni from the core structure. During deactivation, the catalyst transformed either to structures consisting of NiO nanoblocks or hollow NiO shells. The phase transformations occurring during deactivation were associated with Ni diffusion processes that are driven by light illumination.

© 2015 Elsevier B.V. All rights reserved.

## 1. Introduction

Due to the finite supply of fossil fuels and their negative impact on the environment, it is potentially attractive to utilize sun light and water, which are ultimately clean and abundant, to produce energy without contributing to greenhouse gas emission. Water splitting using particulate photocatalysts is one potentially promising method for converting and storing solar energy in the form of H<sub>2</sub> molecules, which can then be used directly in hydrogen fuel cells [1,2] or to produce other fuels from recycled CO<sub>2</sub> [3]. In one approach, a light harvesting inorganic semiconductor with valence and conduction band edges that straddles the electrochemical potentials for water reduction and oxidation is employed [4]. This semiconductor must be stable under reaction conditions and not undergo photocorrosion. Furthermore, suitable co-catalysts are added to the surface of the semiconductor which provide reaction sites and decrease the water reduction/oxidation activation energies resulting in significant improvement of the photocatalytic activity [5].

The free energy change for the uphill reaction of water decomposition is 1.23 eV but overpotentials need to be taken into consideration thus the practical energy needed to drive the reaction is reported to be 1.6–2.4 eV [6,7]. Tantalum oxide and many

tantalite-based systems, which have a band gap of about 4 eV, have been reported to show extraordinarily high activities and quantum yields when decomposing water under ultraviolet (UV) illumination [8–11]. Although pure tantalum oxide shows some photocatalytic activity, loading with a nickel-based co-catalyst improves the initial H<sub>2</sub> production rate by 3 orders of magnitude and results in stoichiometric decomposition of pure water into H<sub>2</sub> and O<sub>2</sub> [12]. Interestingly, in order to have high activity, this co-catalyst has to undergo a pre-treatment consisting of a full thermal reduction in hydrogen followed by partially re-oxidation creating a Ni core–NiO shell morphology. Moreover, noble metal covered with a Cr<sub>2</sub>O<sub>3</sub> layer, which has a similar metal-core oxide-shell structure, is also a very efficient co-catalyst for overall water splitting. It is argued that this co-catalyst structure will not only catalyze the forward reaction but also suppress the backward reaction in which water is formed by combining H<sub>2</sub> and O<sub>2</sub> [5,13].

A detailed atomic-level understanding of the relationship between the catalyst microstructure and the photocatalytic reactivities has not yet been fully explored. Transmission electron microscopy (TEM) is a powerful approach to elucidate atomic level structure and composition providing a nano-level view of the evolution of the catalysts. Correlating the microstructures of the semiconductor, co-catalyst and their interfaces with reactivities should give insights on both reaction and deactivation mechanisms.

In this work, a series of different Ni core–NiO shell co-catalysts were prepared on Ta<sub>2</sub>O<sub>5</sub> substrate particles. The catalytic behavior of the material may be greatly influenced by changes in the

\* Corresponding author. Tel.: +1 4809652934; fax: +1 4809659321.  
E-mail address: [CROZIER@asu.edu](mailto:CROZIER@asu.edu) (P.A. Crozier).

co-catalysts microstructure. One way to modify and tune the co-catalysts structure is by changing the heat treatment conditions during the preparation of the material. This provides an opportunity to correlate changes in activity with relatively well-defined changes in structure allowing fundamental information on structure–reactivity relations to be determined. The photocatalytic activities of all the co-catalysts were measured and compared. TEM was employed to directly observe the changes of the microstructure of the material. By varying the co-catalyst structure in a controlled way and correlating the photocatalytic activity with the structure of both fresh and de-activated photocatalysts, we can obtain a deeper insight on structure–reactivity relationships. The fundamental information derived from these experiments can provide guidance to future improvements in the design of the co-catalyst structure and composition.

## 2. Experimental

### 2.1. Materials preparation

NiO (1 wt%) was loaded on Ta<sub>2</sub>O<sub>5</sub> photocatalyst powders (Aldrich; 99.99%) using an impregnation method from an aqueous solution of Ni(NO<sub>3</sub>)<sub>2</sub>·6H<sub>2</sub>O (Aldrich; 99.999%). Different subsequent heat treatments were conducted to vary the co-catalyst structures: Sample (i) was reduced at 500 °C with flowing 5% H<sub>2</sub>/Ar for 2 h; Sample (ii), (iii) and (iv) were first reduced under the same condition as Sample (i) and then partially oxidized in 200 torr O<sub>2</sub> for 1 h at 100, 150 and 200 °C, respectively; Sample (v) was oxidized at 500 °C with flowing O<sub>2</sub> for 2 h. The reduction and oxidation steps for the heat treatments are summarized in Table 1.

### 2.2. Photocatalytic test

A beaker-shape glass photo reactor with a total volume of approximately 100 mL was designed and built with a quartz window on the top to minimize the absorption of UV light. The photo reactor was connected to a gas chromatography system (GC Varian 450, PLOT column, TCD, Ar carrier). In a typical test, about 0.08 g of catalyst was suspended constantly in 40 mL of pH 7 DI water using a magnetic stirrer at room temperature. The sealed system was first purged with Ar gas for 20–40 min until no residual air was left in the system as demonstrated by the absence of air peaks in the GC spectrum. The suspension was then irradiated from the top by a xenon lamp (Newport) with a mirror selecting the wavelengths from 260 nm to 320 nm. The incoming photon flux was 21.5 mW/cm<sup>2</sup>. Due to the current set up of the photo reactor system, the H<sub>2</sub> and O<sub>2</sub> gases released from water were constantly

carried away by flowing Ar gas and every 10 min the gas mixture was sampled in GC. An H<sub>2</sub> calibration was obtained by measuring peak intensities from H<sub>2</sub>/Ar mixtures of well-defined compositions and flow rates. Therefore, H<sub>2</sub> production rate at each time point can be calculated and plotted. Our current system had very poor sensitivity to O<sub>2</sub> gas because of both the design of our flow reactor and because Ar was used as the carrier gas. Theoretically, the O<sub>2</sub> production should be half of the H<sub>2</sub> production during water splitting but this level was below the detection limit of the current set up. For this reason, we focus only on H<sub>2</sub> evolution in the current work.

### 2.3. TEM characterization

An aberration corrected FEI Titan (300 kV) was used to examine the atomic structure of the co-catalyst on Ta<sub>2</sub>O<sub>5</sub>. The fresh powder catalysts were first imaged before any catalytic tests were conducted. After exposure to water and UV light, the same materials were again imaged to determine the structural evolution that took place under photoreaction conditions.

## 3. Results

### 3.1. Photocatalytic activity

Fig. 1a shows the H<sub>2</sub> production rates of the catalysts as a function of time after starting the UV illumination. After the UV light was turned on, significant H<sub>2</sub> was detected within 10 min and it usually took 20–30 min for the H<sub>2</sub> production rate to reach its maximum. This incubation behavior was believed to be partly associated with the time needed for the evolved H<sub>2</sub> to be mixed with the flowing Ar in the head space above the water and carried to the GC. Sample (v), which was oxidized to NiO at 500 °C, showed no activity. Sample (i) to (iv), produced H<sub>2</sub> at different rates but showed similar variations in activity with time. Sample (i) has the lowest H<sub>2</sub> production rate (64 μmol/h/g), while Sample (iv) had the highest by a factor of 3 (189 μmol/h/g). Samples (i)–(iii) de-activate in the same way with their activities dropping by 50% in 140 min. Interestingly, in addition to having the highest activity, Sample (iv) showed a much longer deactivation time and took 360 min to drop to 50% of the maximum activity (Table 2). There was about 3.8 μmol (0.2 mg) Ni loaded on Sample (iv) initially and 389.6 μmol H<sub>2</sub> was produced till the catalyst deactivated to 20% of its maximum activity. Thus an estimation can be made that 1 mg initial Ni co-catalyst should at least generate 1950 μmol H<sub>2</sub> before the activity drops to zero. Furthermore, pH values of a suspension of Sample (iv) in water before and after exposure to UV light for 5 h were measured and they were both in the range of 7–7.5.

**Table 1**  
Heat treatment conditions for different co-catalysts.

Sample	(i)	(ii)	(iii)	(iv)	(v)
Name	Ni–NiO/Ta <sub>2</sub> O <sub>5</sub> OR <sup>a</sup>	Ni–NiO/Ta <sub>2</sub> O <sub>5</sub> O100	Ni–NiO/Ta <sub>2</sub> O <sub>5</sub> O150	Ni–NiO/Ta <sub>2</sub> O <sub>5</sub> O200	NiO/Ta <sub>2</sub> O <sub>5</sub> O500
Reduction step	500 °C, 2 h, flowing H <sub>2</sub> /Ar				–
Oxidation step	–	100 °C, 1 h, 200 torr O <sub>2</sub>	150 °C, 1 h, 200 torr O <sub>2</sub>	200 °C, 1 h, 200 torr O <sub>2</sub>	500 °C, 1 h, flowing O <sub>2</sub>

<sup>a</sup> OR means exposure to O<sub>2</sub> in air at room temperature.

**Table 2**  
Activity and structure data of different co-catalysts.

Sample	(i)	(ii)	(iii)	(iv)	(v)
Name	Ni–NiO/Ta <sub>2</sub> O <sub>5</sub> OR	Ni–NiO/Ta <sub>2</sub> O <sub>5</sub> O100	Ni–NiO/Ta <sub>2</sub> O <sub>5</sub> O150	Ni–NiO/Ta <sub>2</sub> O <sub>5</sub> O200	NiO/Ta <sub>2</sub> O <sub>5</sub> O500
Maximum H <sub>2</sub> production rate (μmol/h/g)	64 ± 3	93 ± 3	165 ± 12	189 ± 3	0
Reaction time for 50% maximum activity (min)	120 ± 10	120 ± 10	140 ± 10	360 ± 10	–
Average particle size (nm)	10.6 ± 4.8	11.4 ± 4.0	12.9 ± 4.2	19.0 ± 9.1	10.3 ± 2.3
Average oxide shell thickness (nm)	–	2.0 ± 0.5	2.4 ± 0.5	6.4 ± 2.5	–
Average oxide shell thickness/particle size percentage	–	19 ± 5%	19 ± 4%	34 ± 12%	–

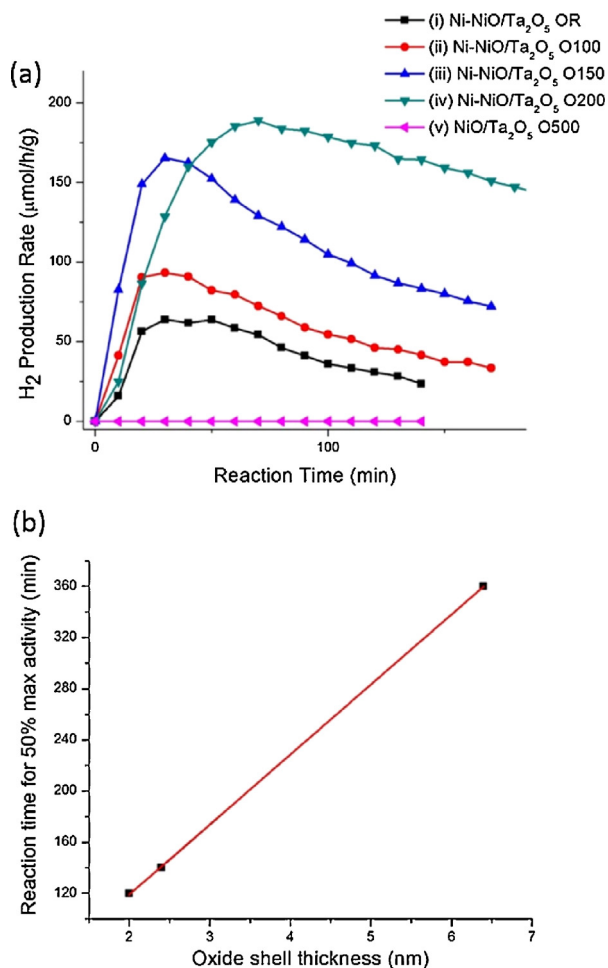


**Fig. 1.** (a) H<sub>2</sub> production rate vs. reaction time of Samples (i)–(v). (b) Reaction time for 50% drop in activity (relative to maximum) vs. oxide shell thickness of Samples (ii)–(iv).

### 3.2. Initial catalyst structures

Fig. 2 shows the variation in the structures of the initial co-catalysts for the 5 materials. Although Sample (i) was not oxidized at elevated temperature in the furnace, it was exposed to air and small nickel oxide domains were formed on parts of Ni metal surfaces confirmed by fast Fourier transform (FFT) (Fig. 2a). The catalytic activity arises because of the existence of both metallic and oxide phases *via* the mechanism discussed in Section 4.1. As the oxidation temperature goes up, Sample (ii) and (iii) show typical core–shell structures where the oxide shell covers the entire Ni metal core in most of the particles. Twin boundaries can often be observed in the metal phase. Sample (iv) shows the most complicated structure where the metal core and the oxide shell are difficult to differentiate presumably because of the low contrast difference between the smaller metallic Ni phase against the larger NiO phase. However FFT analysis of the high resolution transmission electron microscopy (HRTEM) images reveals that both metal and oxide phases are present. Since Sample (v) was oxidized at high temperature with no reduction step, NiO particles arise on the surface of Ta<sub>2</sub>O<sub>5</sub> with NiO (200) planes present as the surface termination facets.

The particle sizes and the oxide shell thicknesses were measured from the HRTEM images for each catalyst, with average values and errors listed in Table 2. The errors come from the heterogeneity of the co-catalyst morphology. Generally speaking, the average particle size as well as the oxide shell thickness increased

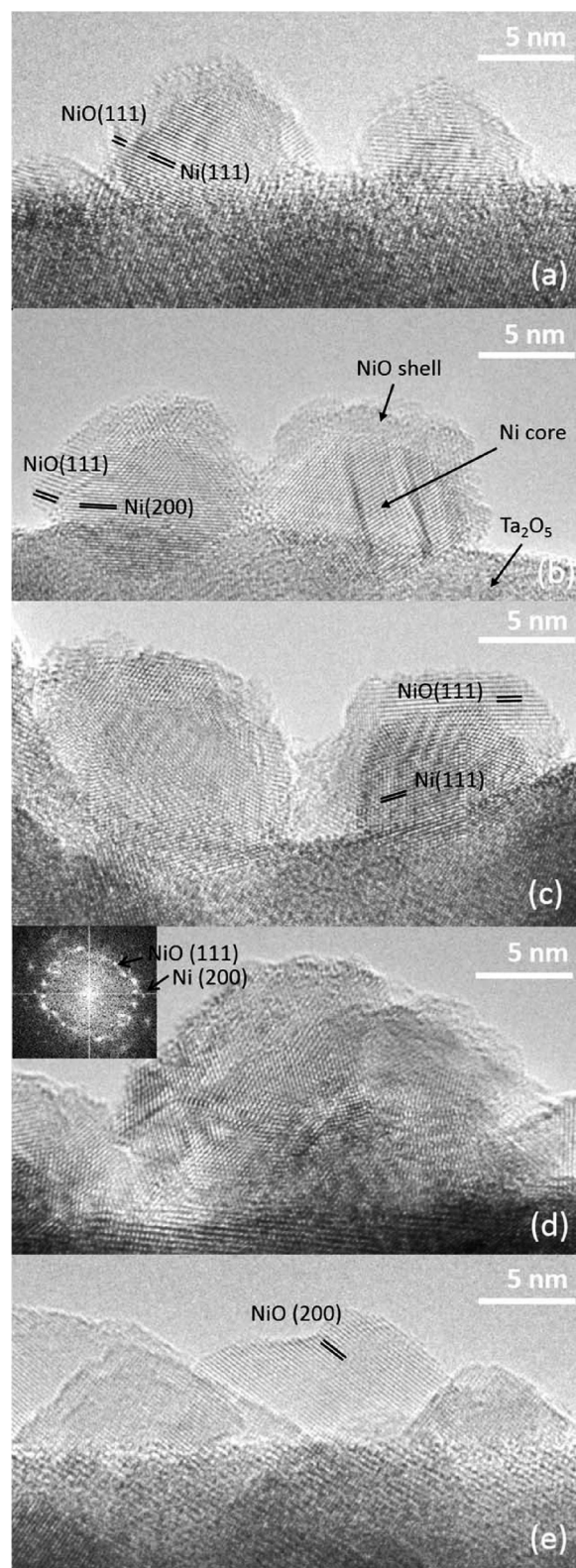


**Fig. 2.** Image (a)–(e) show initial co-catalyst structures of Samples (i)–(v) at the same magnification. (a) Co-catalyst of Sample (i) was mainly Ni metal with a thin layer of native NiO; (b) and (c) clear Ni core–NiO shell structures were observed for Samples (ii) and (iii); (d) most active Sample (iv) showed complicated structure with presence of both Ni and NiO phases; (e) pure NiO particles were observed on Sample (v).



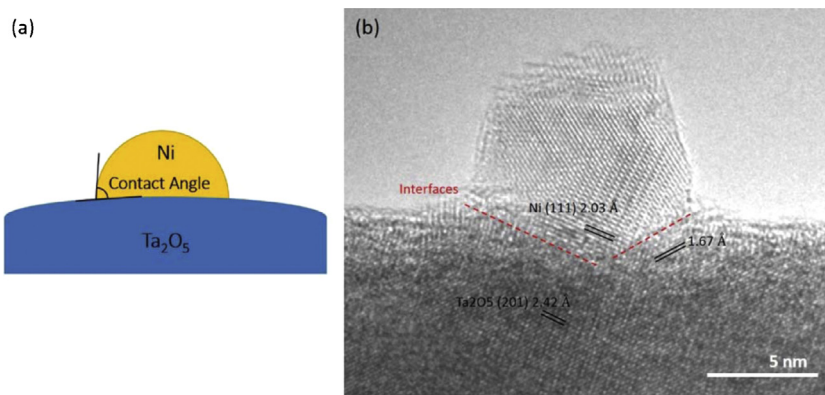


**Fig. 3.** (a) Schematic graph showing the contact angle between Ni particle and Ta<sub>2</sub>O<sub>5</sub> substrate. (b) Typical Ni metal/Ta<sub>2</sub>O<sub>5</sub> semiconductor interface structure.

with increasing oxidation temperature. More specifically, comparing Samples (i)–(iii), a rise in oxidation temperature results in a small change in particle size and oxide shell thickness. Interestingly, this was accompanied by an almost three times increase in the maximum H<sub>2</sub> production. For Sample (iv), a further increase in oxidation temperature results in significant particle growth and a thicker oxide shell but little increase in the maximum H<sub>2</sub> production rate. However, this sample showed improved long term stability with a significant increase in the time for the activity to drop by 50%.

As the oxidation time associated with catalyst preparation increases, the interfaces between Ta<sub>2</sub>O<sub>5</sub> (which has an orthorhombic structure) and the Ni–NiO (which have cubic structures) core–shell becomes more complex and difficult to clearly observe. Thus, careful interface analysis was conducted on Sample (i) where the interfaces between Ta<sub>2</sub>O<sub>5</sub> and Ni metal could be viewed in projection without NiO overlayers. The Ni metal/Ta<sub>2</sub>O<sub>5</sub> orientational relationship and interface structure determined from this sample should be similar to those in the gently oxidized samples assuming the buried Ni metal/Ta<sub>2</sub>O<sub>5</sub> interface does not significantly change. The average contact angle of between the Ni and Ta<sub>2</sub>O<sub>5</sub> (as demonstrated in Fig. 3a) is  $87 \pm 9^\circ$  for this sample. A typical interface structure is shown in Fig. 3b where the relative angles between

Ni and Ta<sub>2</sub>O<sub>5</sub> lattice fringes are commonly observed. The two flat interfaces are parallel to two sets of Ta<sub>2</sub>O<sub>5</sub> lattice fringes with d-spacings of 2.42 Å and 1.67 Å, respectively. The longer interface is almost parallel both to the Ni (111) plane in the metal particle and Ta<sub>2</sub>O<sub>5</sub> (201) plane in the substrate, and it is extended over a distance of 10.6 nm suggesting that it is an energetically favorable configuration. The low interfacial energy together with the fact that Samples (i)–(iv) have high activities, suggests that this coherent interface structure helps with the electron transfer from Ta<sub>2</sub>O<sub>5</sub> substrate to Ni metal co-catalyst.

### 3.3. Used catalyst structures

The deactivation mechanism was investigated by comparing the initial and used catalyst structures of Samples (i) and (iv). Fig. 4 shows the morphology and phase changes of Sample (i) after exposure to UV light and water for 140 min during which the catalytic activity dropped to about 35% of its maximum value. Faceted surface nanodomains (Fig. 4a) and a cluster of multiple blocky nanodomains (Fig. 4b) are observed in the co-catalysts. The changes appear to be correlated with the drop in activity. The morphological similarity suggest that Fig. 4a and b are, respectively, snapshots of the earlier and later stages of structural evolution associated

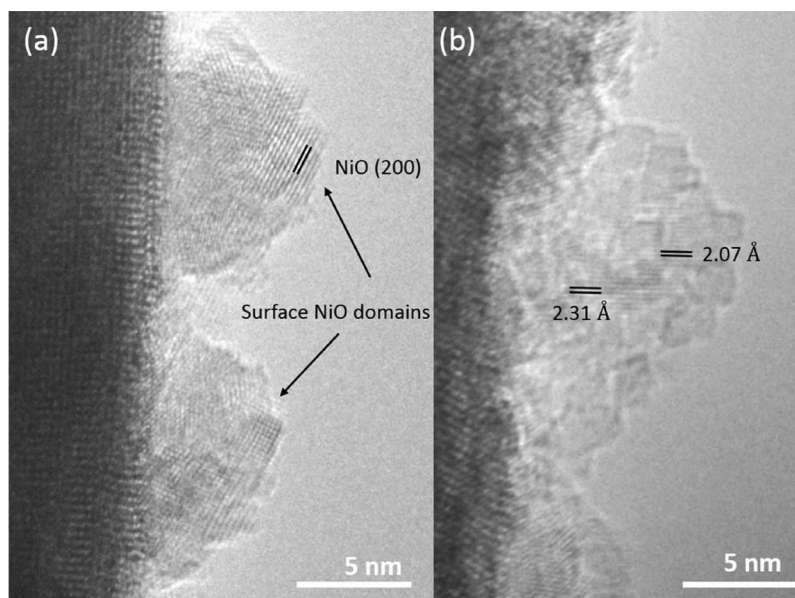


**Fig. 4.** Sample (i) after water and UV exposure for 140 min showing morphology and phase changes: (a) surface of the particles become more faceted, nanodomains and NiO lattice fringes emerge on the surface. (b) The whole particle turns to a cluster of NiO nanoblocks.

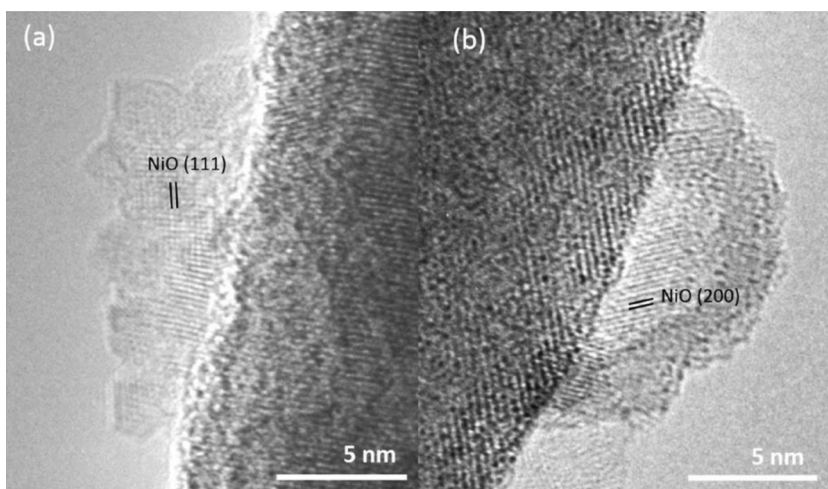


**Fig. 5.** Sample (iv) after water and UV exposure for 16 h showing two types of structures of the used catalyst: (a) blocky NiO nanodomains. (b) Void-shell structure.

with deactivation. FFT analysis of both structures showed that the faceted surface domains and the cluster are NiO with (200) surface termination planes. In addition to forming a cluster, NiO nanodomains were also found finely dispersed on the surface of the  $\text{Ta}_2\text{O}_5$ . Although the surface termination of NiO nanoblocks formed during deactivation is the same as that of NiO particles formed during thermal treatment in Sample (v), they have very different morphologies. It is speculated that during deactivation, surface sites on Ni metal are highly heterogeneous for NiO nucleation and growth. Each active nucleation sites will form a NiO nanodomains and there is not enough thermal energy for NiO nanodomains to sinter and grow into large particles.

After Sample (iv) has been exposed to water and UV light for 16 h, the catalytic activity dropped to 20% of the maximum value. Various changes were observed but the two most dramatic structural changes were: (1) formation of NiO nanodomain cluster (Fig. 5a) as observed in Sample (i); (2) evolution of void-shell structures in which the Ni metal core disappeared leaving a hole in the

center of the NiO shell (Fig. 5b). Some Ni metal was still present in some areas of the used co-catalyst particles and was presumably the reason for continued  $\text{H}_2$  production albeit at a lower level.

Similar structures and morphologies were observed to be associated with the deactivation in all of the catalysts. As illustrated by Sample (i), Ni metal particle is first oxidized to NiO nanodomain on the surface. Then the entire particle changes to multiple NiO nanoblocks. Even with the protection of NiO shell in Samples (ii)–(iv), this type of transformation still occurred during deactivation. The void-shell structure was less frequently observed here than nanoblocks but it was still a significant morphology associated with deactivation observed on a Ni–NiO/ $\text{TiO}_2$  system [14].

Interestingly, some used co-catalysts did not show obvious structural changes implying that there was no charge transfer from the  $\text{Ta}_2\text{O}_5$  to the Ni–NiO. This could be due to a less efficient interface structure for charge transfer, or that the local  $\text{Ta}_2\text{O}_5$  has lower efficiency for electron–hole separation. This phenomenon provides a

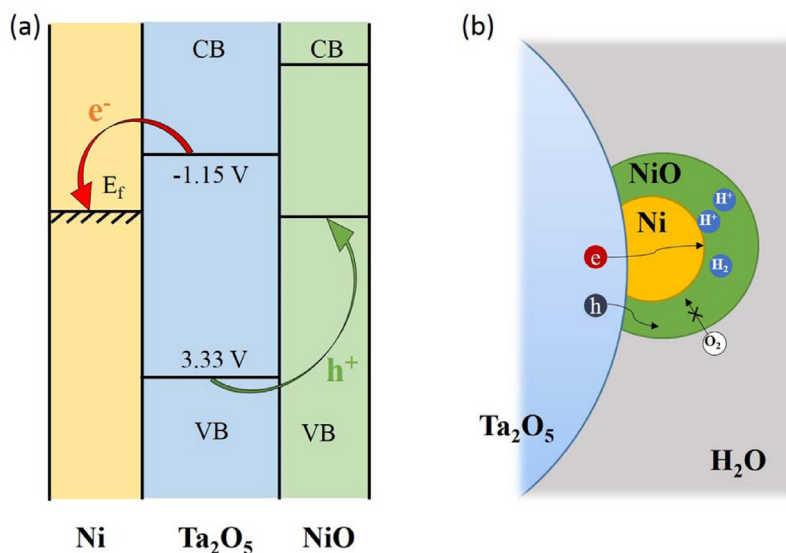


**Fig. 6.** (a) Band alignments between  $\text{Ta}_2\text{O}_5$ , Ni and NiO. The band edge potentials relative to NHE (V) are labeled. (b) Schematic drawing of core-shell structure showing the NiO protective mechanism.

future route to studying the heterogeneity of the catalysts structure on charge transfer.

## 4. Discussion

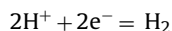
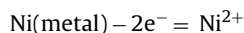
### 4.1. Core-shell water splitting mechanism

The Ni–NiO core-shell structure is believed to thermodynamically enhance the forward water splitting reaction while kinetically limiting the reverse reaction. The process is initiated when the incoming photon (with energy greater than the bandgap of 4.2 eV) is absorbed by the Ta<sub>2</sub>O<sub>5</sub> light harvesting material and electrons are excited into the valence band generating electron–hole pairs. The electrons and holes either recombine or go to different surface reaction sites and may contribute to H<sub>2</sub> and O<sub>2</sub> evolution on the catalyst surface [4,6]. As shown in Fig. 6a, the band alignment of the Ta<sub>2</sub>O<sub>5</sub>, NiO and Ni provides a thermodynamic driving force for the photo-generated electrons to go to the Ni metal, whereas the holes are driven to the valence band of NiO [15,16]. This is supported by the work of Townsend et al. who showed that Ni serves as an electron trap (water reduction site) and NiO serves as a hole trap (water oxidation site) by photovoltage and other experimental measurements [17,18].

However, for the core-shell structure, only the NiO surface is exposed and in contact with water whereas the Ni metal surface is buried below the oxide shell. In fact, Ni metal can catalyze both the water reduction reaction and the water formation reaction (when it is in contact with both H<sub>2</sub> and O<sub>2</sub>) while NiO has been reported to show inhibition behavior for water formation reaction [19,20]. It has been proposed that the oxide shell of the co-catalyst may serve as a protective layer to prevent the backward reaction between H<sub>2</sub> and O<sub>2</sub>. Although this mechanism has been proposed for the noble metal–Cr<sub>2</sub>O<sub>3</sub> co-catalyst system [5,13], it may also work for the Ni metal–NiO shell system which has a similar structure. The protective mechanism of the core-shell structure is illustrated schematically in Fig. 6b. Protons diffuse through the NiO shell and reach the buried Ni–NiO interface, get reduced to H<sub>2</sub> by the photo-generated electrons accumulated in Ni metal. The evolved H<sub>2</sub> then diffuses out through the NiO shell. Meanwhile, O<sub>2</sub> is generated on the surface of NiO by oxidizing H<sub>2</sub>O/OH<sup>−</sup> using the photo-generated holes. It is easy for oxygen to leave the NiO surface and go into solution. Moreover, oxygen cannot diffuse rapidly through Ni and as a result, O<sub>2</sub> is inhibited from reacting catalytically with H<sub>2</sub> on the Ni metal surface to reform water. Thus the reverse reaction is suppressed.

This mechanism suggests an interpretation for why the photocatalytic activities change significantly with varying the extent of oxidation during the catalyst preparation. The increase in the photocatalytic activities from Sample (i) to (iv) results from the increase in the NiO shell thickness which appears to be associated with greater suppression of the reverse reaction. An optimization of the co-catalyst particle size as well as the oxide shell thickness is desired to give the best activity. From this work, the optimum appears to be a particle size of ~20 nm or larger with an oxide shell thickness percentage of 30–40%.

It is possible that the H<sub>2</sub> production is the result of a photochemical rather than a photocatalytic reactions. Such a mechanism has been observed on Ni–NiO core-shell co-catalysts on TiO<sub>2</sub> [14] and involves H<sub>2</sub> production during dissolution of Ni. Specifically, Ni may donate electrons to protons and produces hydrogen, i.e.,



This mechanism can be mostly discounted for the current materials by comparing the number of metallic Ni atoms with the number of molecules of H<sub>2</sub> produced. If we assume that this photochemical reaction is responsible for all the H<sub>2</sub> produced, the total moles of produced H<sub>2</sub> can be estimated based on the amount of initially loaded Ni metal on each sample as shown in Table 3. As the oxidation temperature increases, more Ni is oxidized to NiO so the initial Ni metal decreases from Sample (i) to (iv) leading to a drop of estimated H<sub>2</sub> production. In contrast to this prediction, the H<sub>2</sub> produced increases dramatically in the experiments as the Ni metal content decreases. In the case of Sample (iv), the amount of H<sub>2</sub> detected is 2 orders of magnitude higher than the predicted amount of H<sub>2</sub> amount from the photochemical reaction. For this sample, the photochemical contribution to H<sub>2</sub> production from the mechanism outlined above is negligible, strongly suggesting that the Ni core–NiO shell structure actually catalyzes water splitting.

### 4.2. Deactivation

A common factor in both the blocky and void-shell structure transformations is the loss of the Ni metal phase. As a result, the electrical contact between the metal and semiconductor is lost and thus the number of surface reduction sites decreases leading to the drop in H<sub>2</sub> production rate over time. On the contrary, there was no obvious corrosion of the NiO shell, which may suggest that the Ni loss is independent on pH or chelators along with the fact that the pH of the suspension stayed in the range of 7–7.5 during the reaction. Interestingly, Fig. 1b shows the reaction time for 50% max reactivity depends almost linearly on the oxide shell thickness based on the analysis of Samples (ii)–(iv). It was also observed that exposure of the catalyst to just water in the absence of UV illumination resulted in no significant change in the structure and activity even after several hours, suggesting the deactivation is associated with a light driven diffusion controlled process.

The loss of Ni metal can be explained by two likely mechanisms:

- Photocorrosion of Ni metal in which Ni ions dissolve into the surrounding water. This can be associated with the void-shell formation if the NiO shell is preserved, or the NiO nanoblocks formation if the NiO shell breaks down and changes its morphology. The amount of NiO should not change before and after deactivation for this mechanism.
- Oxidation of Ni metal core to NiO phase. A volume expansion will be associated with this transformation, which could result in local stresses and form NiO nanodomains. In this case, the amount of NiO on the used catalysts would increase.

**Table 3**

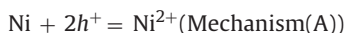
The comparison between estimated H<sub>2</sub> production from photochemical reaction and the actual H<sub>2</sub> production detected by GC till 50% max reactivity.

Sample	Name	Ni (μmol)	Estimated H <sub>2</sub> production from photochemical reaction (μmol)	Actual H <sub>2</sub> production detected by GC till 50% max reactivity (μmol)
(i)	Ni–NiO/Ta <sub>2</sub> O <sub>5</sub> OR	11.6	11.6	8.1
(ii)	Ni–NiO/Ta <sub>2</sub> O <sub>5</sub> O100	5.9–8.2	5.9–8.2	12.1
(iii)	Ni–NiO/Ta <sub>2</sub> O <sub>5</sub> O150	5.9–7.8	5.9–7.8	23.4
(iv)	Ni–NiO/Ta <sub>2</sub> O <sub>5</sub> O200	1.2–6.0	1.2–6.0	126.7



The initial native NiO shell in Sample (i) was very thin but still lots of NiO nanoblocks were found on the used catalyst suggesting that mechanism (B) actually dominates for this sample. Whether mechanism (A) or (B) dominates for Samples (ii)–(iv) remains unclear.

Other than water decomposition, there could be complicated competitive redox reactions occurring in the presence of light and water leading to a rise in the Ni oxidation state. Photochemical reactions, although not the major source of H<sub>2</sub> production, could still occur resulting in formation of Ni ions (mechanism (A)). In addition, taking into account the holes accumulated in the NiO phase and OH<sup>−</sup> in water, other possible reactions are listed below:



For these reactions to occur, certain Ni diffusion must occur to bring Ni into contact with the oxidizing agent and other reactants. Three possibilities are discussed here for facilitating the diffusion processes. The first mechanism is that the H<sub>2</sub> formed at the interface between Ni and NiO may accumulate leading to stress build up resulting in cracks formation and growth in the NiO shell. Ni may then be oxidized *via* contact with water or the produced O<sub>2</sub> molecules. However, this is less likely to occur based on the data obtained from Samples (ii) and (iii). The H<sub>2</sub> production of (iii) is nearly twice as much as that of (ii) which would lead to faster crack formation and growth in NiO. Also, the average oxide shell thickness/particle size percentages of these two samples are similar thus the deactivation time for Sample (iii) should be faster. This hypothesis is contradicted by the observation that the reaction time for 50% max reactivity of Sample (iii) is 20 min longer.

The second possibility is that the initial thermally produced NiO shell could have micropores after the catalyst preparation, providing diffusion pathways for both H<sup>+</sup> and OH<sup>−</sup> to permeate the NiO shell and get into contact with Ni. The incident light deposits energy into the system which triggers the deactivation reactions listed before.

The last possibility considers a Kirkendall type diffusion. The transformation of initial Ni–NiO to a void-shell structure has been previously observed by Chenna et al. in an *in situ* TEM work where Ni metal nanoparticles were oxidized in a well-controlled environment at elevated temperature. The resulting NiO shell structure was explained *via* a Kirkendall mechanism since the diffusion coefficient of Ni cations along the NiO grain boundaries is 8 orders of magnitude higher than that of O anions at 400 °C [21–24]. This mechanism seems likely for producing the hollow NiO shell observed in the deactivated materials. In the current work, the calculated local temperature rise of Ni metal from absorption of the incident light is ~10<sup>3</sup> K/s. However, this excess heat can be carried away by the surrounding oxide thus the co-catalyst stayed at ambient temperature during water splitting. The thermal diffusion rate for both Ni cations and O anions at room temperature is negligible thus the formation of deactivated void-shell structure in this work is not a thermal effect. However, there could be a light driven Kirkendall process where the incident light drives Ni diffusion through the NiO shell. The exact nature of this light driven diffusion process remains unclear at the moment and will be the topic of future research.

## 5. Conclusions

Ni–NiO core–shell co-catalyst structures on Ta<sub>2</sub>O<sub>5</sub> have been investigated for solar H<sub>2</sub> production. Core–shell co-catalysts with different morphologies were produced by varying the heat treatment conditions during catalyst preparation. The morphological changes resulted in large changes in photocatalytic activity. Increased H<sub>2</sub> production was found to be related to an increase in the thickness of NiO shell due to suppression of the back reaction. The best catalyst made so far should at least generate 1950 μmol H<sub>2</sub> with 1 mg initial Ni co-catalyst before it completely deactivates. The core–shell co-catalyst structures deactivated primarily due to a loss of metallic Ni from the core structure. During deactivation, the catalyst transformed either to structures consisting of NiO nanoblocks or hollow NiO shells. The phase transformations occurring during deactivation were associated with Ni diffusion processes that are driven by light illumination. However, the exact nature of this photocorrosion mechanism is not yet well understood.

## Acknowledgement

The support from US Department of Energy (DE-SC0004954) and the use of TEM at John M. Cowley Center for High Resolution Microscopy at Arizona State University is gratefully acknowledged.

## References

- [1] A.J. Bard, M.A. Fox, *Acc. Chem. Res.* 28 (1995) 141–145.
- [2] M. Momirlan, T.N. Veziroglu, *Int. J. Hydrogen Energy* 30 (2005) 795–802.
- [3] G.A. Olah, A. Goepfert, G.K. Surya Prakash, *J. Org. Chem.* 74 (2009) 487–498.
- [4] S. Chen, L.-W. Wang, *Chem. Mater.* 24 (2012) 3659–3666.
- [5] K. Maeda, K. Domen, *J. Phys. Chem. Lett.* 1 (2010) 2655–2661.
- [6] M.G. Walter, E.L. Warren, J.R. McKone, S.W. Boettcher, Q. Mi, E.A. Santori, N.S. Lewis, *Chem. Rev.* 110 (2010) 6446–6473.
- [7] X. Chen, S. Shen, L. Guo, S.S. Mao, *Chem. Rev.* 110 (2010) 6503–6570.
- [8] A. Kudo, *Int. J. Hydrogen Energy* 31 (2006) 197–202.
- [9] A. Kudo, Y. Miseki, *Chem. Soc. Rev.* 38 (2009) 253–278.
- [10] H. Kato, A. Kudo, *Catal. Today* 78 (2003) 561–569.
- [11] S. Ikeda, M. Fubuki, Y.K. Takahara, M. Matsumura, *Appl. Catal. A: Gen.* 300 (2006) 186–190.
- [12] H. Kato, A. Kudo, *Chem. Phys. Lett.* 295 (1998) 487–492.
- [13] M. Yoshida, K. Takanabe, K. Maeda, A. Ishikawa, J. Kubota, Y. Sakata, Y. Ikezawa, K. Domen, *J. Phys. Chem. C* 113 (2009) 10151–10157.
- [14] L. Zhang, Q. Liu, T. Aoki, P.A. Crozier, *J. Phys. Chem. C* (2014).
- [15] W.-J. Chun, A. Ishikawa, H. Fujisawa, T. Takata, J.N. Kondo, M. Hara, M. Kawai, Y. Matsumoto, K. Domen, *J. Phys. Chem. B* 107 (2003) 1798–1803.
- [16] J. He, H. Lindstrom, A. Hagfeldt, S.-E. Lindquist, *J. Phys. Chem. B* 103 (1999) 8940–8943.
- [17] T.K. Townsend, N.D. Browning, F.E. Osterloh, *Energy Environ. Sci.* 5 (2012) 9543–9550.
- [18] H. Kato, et al., *J. Am. Chem. Soc.* 9 (125) (2003) 10.
- [19] Y. Matsumoto, U. Unal, N. Tanaka, A. Kudo, H.J. Kato, *Solid State Chem.* 177 (2004) 4205–4212.
- [20] K.K. Hansen, *J. Appl. Electrochem.* 38 (2008) 591–595.
- [21] S. Chenna, P.A. Crozier, *Micron* 43 (2012) 1188–1194.
- [22] A. Atkinson, R.I. Taylor, *J. Mat. Sci.* 13 (1978) 427–432.
- [23] A. Atkinson, D.P. Moon, D.W. Smart, R.I. Taylor, *J. Mater. Sci.* 21 (1986) 1747–1757.
- [24] R. Peraldi, D. Monceau, B. Pieraggi, *Oxid. Met.* 58 (2002) 275–295.